

Article

Underwater Superoleophobicity Induced by the Thickness of the Thermally Grown Porous Oxide Layer on C84400 Copper Alloy

Aniedi Nyong * and Pradeep Rohatgi

Department of Materials Engineering, University of Wisconsin-Milwaukee, Milwaukee 53211, WI, USA; E-Mail: prohatgi@uwm.edu

* Author to whom correspondence should be addressed; E-Mail: aenyong@uwm.edu or aniedinyong@yahoo.com; Tel.: +1-414-514-0491. Fax: 414-229-6958

Received: 30 September 2013; in revised form: 16 January 2014 / Accepted: 22 January 2014 /

Published: 20 February 2014

Abstract: The underwater contact angle behavior on oxide layers of varying thicknesses was studied. These oxide layers were grown by thermally oxidizing C84400 copper alloys in N₂-0.75 wt.% O₂ and N₂-5 wt.% O₂ gas mixtures at 650 °C. Characterization of the oxidized specimens was effected using X-ray diffraction, scanning electron microscope (SEM) and contact angle goniometer. The results from the X-ray diffraction analyses confirmed the formation of CuO, ZnO and PbO. The average sizes of the oxide granules were in the range of 70 nm to 750 nm, with the average thickness of the oxide layer increasing with the increase in the weight percent of oxygen in the N₂-O₂ gas mixtures. The results showed that the oxide layer growth followed the parabolic law. The underwater oil contact angles increased, due to the change in the surface morphology and porosity of the oxide layer. The small sizes and irregular packing of the oxide granules cause hierarchical rough surface layers with pores. The estimated pore sizes, in the range of 88 ± 40 to 280 ± 76 , were predominant on the oxide layers of the samples processed in the N₂-5 wt.% O₂ gas mixture. The presence of these pores caused an increase in the porosities as the thickness of the oxide layers increased. At oxide layer thickness above 25 microns, the measured contact angle exceeded 150° as underwater superoleophobicity was recorded.

Keywords: thermal oxidation; superoleophobicity; oxide layer; porosity

1. Introduction

Superoleophobic surfaces refer to those surfaces that display contact angles that are greater than 150° along with low contact angle hysteresis for low surface tension liquids, such as oils and alcohols [1]. The contact interface for oil on a superoleophobic surface can either be solid-air or solid-water interface, depending on the media the surfaces are placed. For the latter, the interface can effectively be achieved under water. To this end, attention has increasingly been paid to the design of underwater superoleophobic surfaces, due to their potential application in anti-fouling coatings [2], oil-water separation [3], as well as anti-bioadhesion surfaces [4].

Various approaches have been used to achieve superoleophobicity on surfaces under water. Some of these approaches include fabrication of re-entrant structures on surfaces of substrates [5], complicated etching methods such as lithography and anodization [6].

Recently, however, high energy materials, such as oxides, have been used to achieve underwater superoleophobicity. For instance, underwater superoleophobicity has been achieved by coating stainless steel mesh with aligned ZnO nanorod film [7]. The ZnO nanorod coating was generated by a two-step process which involved dipping the steel mesh in ZnO sol gel and annealing at 450°C . Underwater superoleophobic surfaces on copper substrate coated with copper oxide, formed as a product of aqueous corrosion in ammonium hydroxide solution, has been created [8]. Liu and his co-workers further reported that the high amount of CaCO_3 as well as the micro-/nano-hierarchical structures of clam shells were responsible for the underwater, low adhesive superoleophobicity of clam shells [9]. Other examples include high energy organic-based materials that have been used to achieve underwater superoleophobicity. In this regards, high-energy poly-(*N*-isopropylacrylamide) hydrogel has been used to achieve superoleophobicity. The hydrogels were used to construct fish-like surfaces with micro-/nano-structures that showed robust underwater superoleophobicity [10].

The process of thermal oxidation can be used to form oxide surface layers of varying thickness, morphology and chemical composition. These variations of the properties of the oxide surface layers can be induced by the control of the thermal oxidation conditions and can therefore be used to generate and sustain the superoleophobicity of metal alloys under water. The formation, thickness, chemical features and the morphology of oxide layers on metal alloys is dependent on the alloy composition, oxidation temperature, time of thermal oxidation, as well as the partial pressure and concentration of oxygen [11]. This paper addresses the effect of the thickness and surface morphology changes of thermally-grown oxide layers on the underwater contact angle and superoleophobic behavior of oil on the surfaces of C84400 copper alloy.

The C84400 copper alloy is a typical leaded brass that contains copper, lead, zinc and tin [12]. This copper alloy is commonly used as plumbing fittings. The bio-fouling of such plumbing parts constitutes a serious problem that can be reduced if their surfaces exhibit underwater superoleophobicity [13]. Through the use of oxidizing gas mixtures that contain different amounts of oxygen during thermal oxidation, the thickness of the oxide layer can be controlled and different oxide morphologies generated to study the contact angle behavior of oil drops underwater. Though underwater superoleophobicity induced by high energy oxides have been reported, we report here, for the first time, such underwater superoleophobicity driven by the thickness of a porous, thermally-grown oxide layer.

2. Materials and Experimental Method

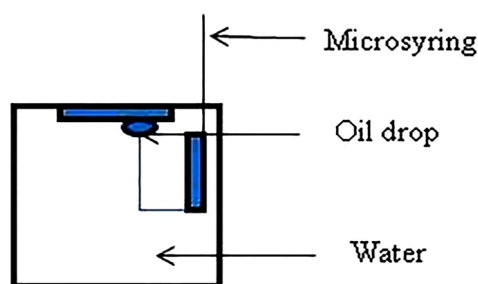
2.1. Materials

The copper alloy used in these experiments is the C84400 copper alloy, obtained from Badger Meter (Milwaukee, WI, USA). The composition of the C84400 copper alloy include the following elements in their respective weight percentages; copper (81 wt.%), lead (7 wt.%) tin (3 wt.%) and zinc (9 wt.%). The thermal oxidation of the samples was carried out in two different N₂-O₂ gas mixtures obtained from Praxair (Brookfield, CT, USA). These N₂-O₂ gas mixtures were N₂-0.75 wt.% O₂ and N₂-5 wt.% O₂. The choice of these gas mixtures is to effect varying oxygen concentration within the furnace during the thermal oxidation process. The oil used in measuring the contact angle was soybean oil, a typical vegetable oil with a surface tension value of 27.6 mN/m.

2.2. Experimental Method

The leaded semi-red C84400 copper alloy was sectioned into 15 mm × 10 mm × 3 mm pieces. These samples were then polished until fine surfaces were obtained by using a soft cloth impregnated with a 1-micron alumina slurry. The polished samples were then washed in distilled water and dried in air. To establish the oxidation atmosphere, the various N₂-O₂ gas mixtures were flowed through the furnace with an inlet and outlet for the introduction of the oxidizing gas mixtures, at a rate of 4.5 liters per minute. The temperature of the furnace was ramped up to 650 °C, and after a time period of 10 min for the homogenization of the oxidization gas mixture within the furnace, the samples were pushed into the hot zone of the furnace. The times set for the thermal oxidation process were 1, 2 and 3 h, respectively, and the process was done at atmospheric pressure. After thermal oxidation for the specified time, the samples were slowly removed and allowed to cool in an evacuated bell jar.

Figure 1. Experimental set up for the measurement of the oil drop contact angle under water.



2.3. Characterization Technique

The characterization of the thermally oxidized surfaces of the C84400 copper alloy involved the determination of the values of the average surface roughness, R_a , using a 2-D surface profilometer (Phase II, SRG-4500; Phase II, Upper Saddle River, NJ, USA). The average surface roughness, R_a , of the surfaces was measured at five different places, and the average was evaluated. The oil contact angles under water were measured by placing the samples slightly below the surface of pure distilled water in a clean, transparent container. The drops of oil with a volume of about 5 μ L were placed on the surface using a micro-syringe, as illustrated in Figure 1.

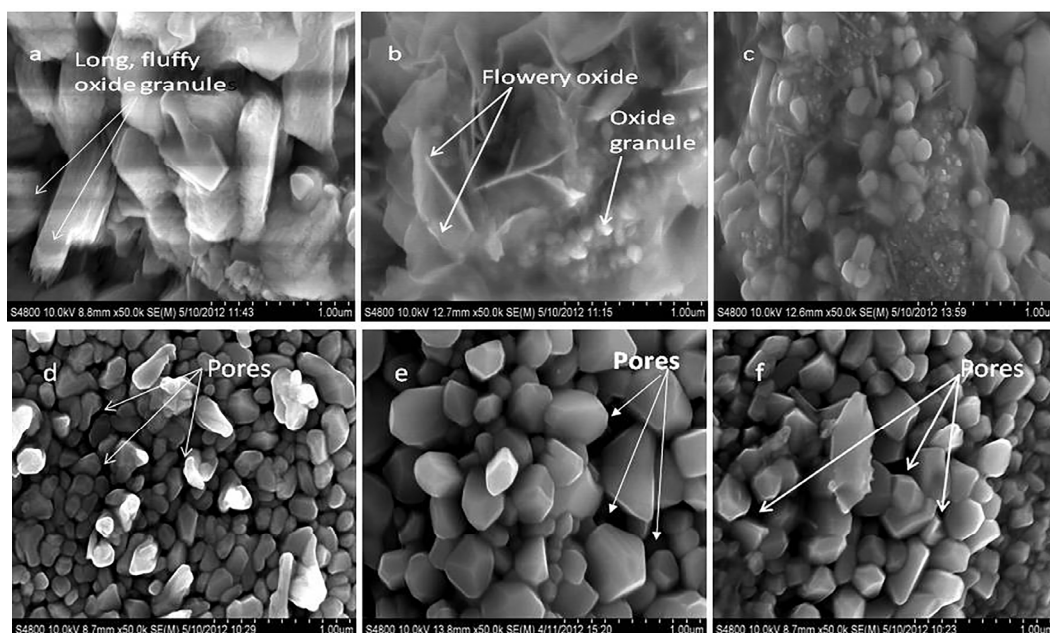
The contact angles of these oil drops were measured at room temperature using a contact angle goniometer (Rame Hart 250 model goniometer, Ramé-Hart instrument company, Succasunna, NJ, USA). The nature and morphology of these thermally oxidized surfaces of the C84400 samples were evaluated with the Hitachi-S4800 scanning electron microscope (Hitachi High-Technologies Corporation America, Inc., Schaumburg, IL, USA), equipped with an energy dispersive X-ray (EDX) probe. X-ray diffraction (Scintag 2000 X-ray diffraction equipment, Scintag Inc., Livermore, CA, USA) and the energy dispersive X-ray analyses were also used to study the chemical composition of the surfaces after the thermal oxidation process. These X-ray analyses were carried out at a 2θ range of 10° – 70° , with a continuous count rate of $2^\circ/\text{min}$ using the $\alpha\text{-Cu}$ emission of a wavelength of 1.54 \AA .

3. Results and Discussion

3.1. Surface Morphology Examination

The thermal oxidation of the samples in the different oxidizing gas mixtures generated various oxide surface morphologies on the C84400 substrate. These different morphologies are as shown in Figure 2.

Figure 2. Scanning electron microscope (SEM) images of thermally oxidized C84400 in different oxidizing atmospheres: (a,b,c) 1, 2, 3 h in N_2 -0.75 wt.% O_2 ; and (d,e,f) 1, 2 and 3 h in N_2 -5 wt.% O_2 gas mixtures, respectively, at 650°C .

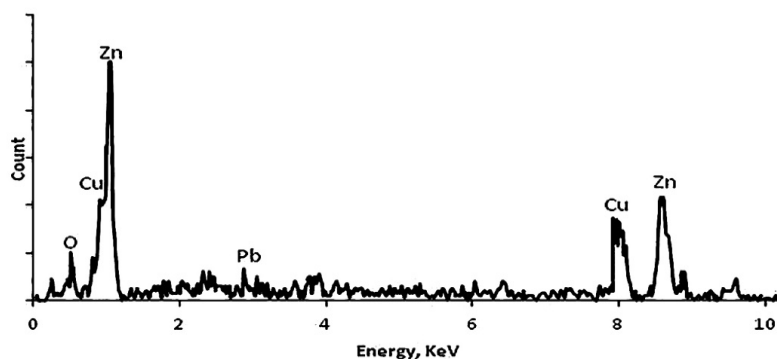


From the observed morphologies, the shapes of the various oxides formed were irregular in nature, as the nucleation and growth process were affected by the thermal oxidation conditions. Long, fluffy oxide granules were formed after 1 h of thermal oxidation in the N_2 -0.75 wt.% O_2 gas mixture. At 2 h of thermal oxidation, the morphology of the oxidized surface layer showed flowery oxide features interspersed with spherically-shaped oxide granules. This morphology can be understood, since low

oxygen partial pressure to a certain range is expected to decrease the oxide nucleation rate. Under such conditions and with fewer nucleation sites, due to the low amount of oxygen, the oxides grew laterally into these flowery forms. The measured width of the flowery oxides formed was an average of 85 ± 9 nm in thickness. However, more defined oxide granules were formed after the 3 h of the thermal oxidation process, with an average oxide granule size of 110 ± 40 nm.

An appraisal of the chemical composition of these flowery oxides formed after 2 h of thermal oxidation in the N_2 -0.75 wt.% O_2 gas mixture by energy dispersive X-ray analysis showed that they consisted of zinc, lead, copper and oxygen in the weight percentage of 34.75 wt.%, 33.38 wt.%, 6.40 wt.% and 11.78 wt.%, respectively. This chemical composition showed that these flowery oxides were essentially formed from merged thin oxide flakes of zinc, copper and lead. The EDX spot analysis is shown in Figure 3.

Figure 3. Energy dispersive X-ray analysis of the flowery oxides formed on the thermal oxidation of C84400 copper alloy in the N_2 0.75 wt.% O_2 gas mixture for 2 h.



In the N_2 -5 wt.% O_2 gas mixture, the oxide granules on the surfaces of the samples were more consistent in form and size. The increase in the weight percentage of oxygen caused an increase in the number of nucleation sites, which resulted in a more regular and consistent morphology. No flowery oxide morphology was formed on the samples oxidized in the gas mixture with five weight percent of oxygen. The sizes of the oxide granules formed were consistent and comparable in the range of 70 ± 22 nm to 130 ± 15 nm, with the oxide granules progressively becoming smaller as the time for the thermal oxidation increased. The sizes of these oxide granules formed in the N_2 - O_2 gas mixtures are stated in Table 1.

Table 1. The average oxide granule size, α ; the fractional surface area, f_{so} ; the estimated pore size, D ; and the calculated oxide layer porosity, ϕ .

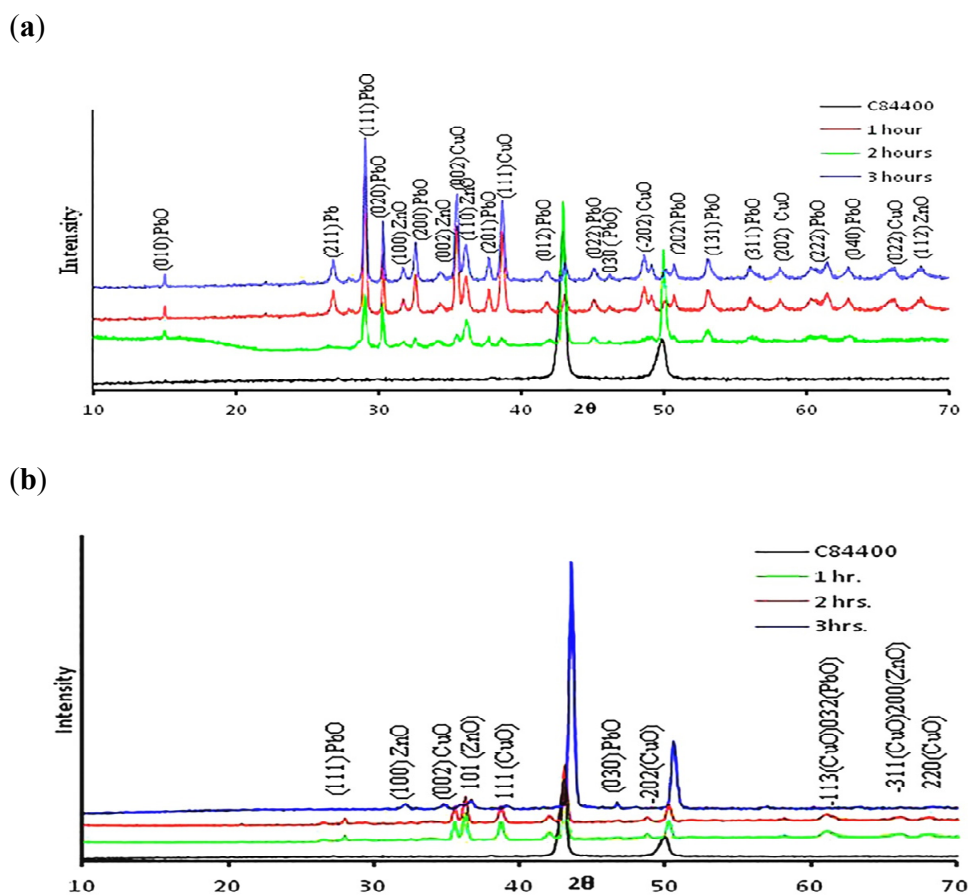
N_2 - O_2 gas mixture	Time (h)	Average granule size, α (nm)	Fractional surface area of oxide, f_{so}	Estimated pore size, D (μ m)	Calculated porosity, ϕ
N_2 0.75 wt.% O_2	1	750 ± 50	0.74	0.19 ± 0.05	0.06
	2	130 ± 15	0.67	-	-
	3	110 ± 40	0.58	0.09 ± 0.03	0.27
N_2 5 wt.% O_2	1	134 ± 45	0.61	0.517 ± 0.13	0.49
	2	101 ± 43	0.32	0.587 ± 0.10	0.58
	3	70 ± 14	0.11	0.509 ± 0.23	0.64

Further appraisal of the surfaces showed a wide distribution of pores in the oxidized surface layers. These pores were quite conspicuous on the samples surfaces that were thermally oxidized in the N₂-5 wt.% O₂ gas mixture. The sizes of the pores were measured from the scanning electron microscope and are stated in Table 1. The distribution of the pores was quite insignificant in the samples that were oxidized in the N₂-0.75 wt.% O₂ gas mixture. The SEM images in Figure 2 show these randomly distributed pores present on the oxide layers of the C84400 copper alloy samples after they were thermally oxidized in the in the N₂-5 wt.% O₂ gas mixture.

3.2. X-ray Diffraction Phase Analyses

The phase analyses of the surfaces of the samples of the C84400 copper alloy, thermally oxidized in the N₂-O₂ gas mixtures at 650 °C, showed also the presence of various diffraction planes of the oxides formed, as presented in Figure 4. The diffraction peaks corresponded to the (002), (111), (022), (220), (−202), (202), (−113) and (−311) planes of CuO; the (100), (002), (110),(101), (200) and (112) planes of ZnO; and the (010), (020), (201), (012), (022), (202), (131), (111), (311), (222), (032) and (040) planes of PbO. These identified planes confirmed the presence of monoclinic CuO, hexagonal ZnO and orthorhombic PbO on the oxidized surfaces, based on Powder Diffraction File (PDF) cards numbers 80–1917, 36–1451 and 38–1477 for PbO, CuO and ZnO, respectively.

Figure 4. (a) X-ray diffraction pattern of thermally oxidized C84400 copper alloy samples in N₂-0.75 wt.% O₂; (b) X-ray diffraction pattern of thermally oxidized C84400 copper alloy samples in N₂-5 wt.% O₂.



From the X-ray analyses presented in (Figure 4a,b), it is observed that a lesser number of the oxide planes diffracted the X-rays in samples oxidized in N₂-5 wt.% O₂ compared to those oxidized in N₂-0.75 wt.% O₂ over the same time period. The X-ray diffraction peaks were broad, due to the very small sizes of the oxides formed. Based on the XRD data, no Cu₂O was formed on the oxide layers in both N₂-O₂ gas mixtures used. All the copper oxide exists in the form of CuO. The miller-indexed (002) and (111) reflections for CuO have the highest intensities, indicating that these were the preferred crystal planes of the oxides in the samples that were thermally oxidized in the N₂-0.75 wt.% O₂ gas mixture. The preferred planes for the PbO and ZnO equally formed during the thermal oxidation of the samples in N₂ 0.75 wt.% O₂ gas mixture were (111) and (110) Miller-indexed reflections, respectively. In the N₂ 5 wt.% O₂, the faster oxidation rate resulted in a faster nucleation and growth of the oxide layer, causing lesser oxide planes to occur.

The Gibb's free energy of formation, ΔG , of ZnO, CuO and PbO shows that the formation of ZnO is the most energetically favorable at the process temperature of 650°. In copper alloys, there is a critical zinc concentration above which only the oxidation of the zinc will occur. This critical concentration estimated by Wagner [14] is 15 at.% Zn. The concentration of zinc in the C84400 copper alloy is 8.9 at.% (9 wt.%), which is lower than the critical concentration for the formation of only ZnO from the oxidation of zinc. Hence, CuO was equally oxidized from Cu₂O during the thermal oxidation. Lead has a very low melting point (327.3 °C) [15]. To this extent, the lead particles in the alloy microstructure melted quickly in the process of thermal oxidation and segregated to the surface, where it was easily oxidized to PbO, as noted by the X-ray diffraction analysis.

3.3. Oxidation and Mechanism of Growth of the Oxide Layer

The cross-sectional thicknesses of the oxide layers grown on these substrates at 650 °C were examined with the Hitachi S-4800 scanning electron microscope, as shown in Figure 5. The well-defined oxide layers for the samples that were oxidized in N₂ 0.75 wt.% O₂ and N₂ 5 wt.% O₂ showed some cracks of the layers from the substrate surface, in some cases. These cracks were found at the interfaces between the substrates and the oxide layer. At a temperature of 650 °C, the differences in the thermal expansivities between the oxides forming in the oxide layer and the C84400 copper alloy substrate induce stresses and cracks. In this instance, the coefficient of thermal expansion (CTE) of the ZnO, CuO and PbO are $4.0 \times 10^{-6}/^{\circ}\text{C}$, $4.3 \times 10^{-6}/^{\circ}\text{C}$ and $9.4 \times 10^{-6}/^{\circ}\text{C}$ [16,17], respectively, and are quite lower than the linear expansivity of the C84400 copper alloy, which has a value of $18.8 \times 10^{-6}/^{\circ}\text{C}$ [18]. The oxide layer experienced compressive stresses, as the C84400 copper alloy expanded faster at the high temperature used in the oxidation, thus causing the cracks observed. Equally, some of the observed cracks may be due to the effect of wear during the polishing of the cross-sections for SEM examination.

The values of the average oxide layer thickness, measured from the SEM images in Figure 5, are stated in Table 2. The oxidation rate at which these various oxides were formed was evaluated based on the oxide layer thickness as a function of the thermal oxidation time at 650 °C using the parabolic relation [19] in Equation (1).

$$X^2 = K_p t \quad (1)$$

Figure 5. SEM images showing the oxide layer thickness and the measured oil contact angles under water. (a–c) Oxidized in the N₂ 0.75 wt. % O₂ gas mixture; (d–f) oxidized in the N₂ 5 wt.% O₂ gas mixture. The insert is the underwater contact angle of oil.

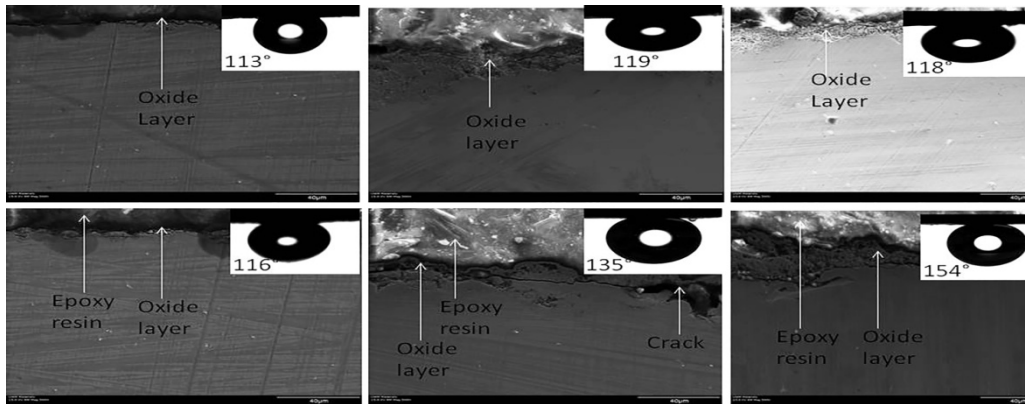
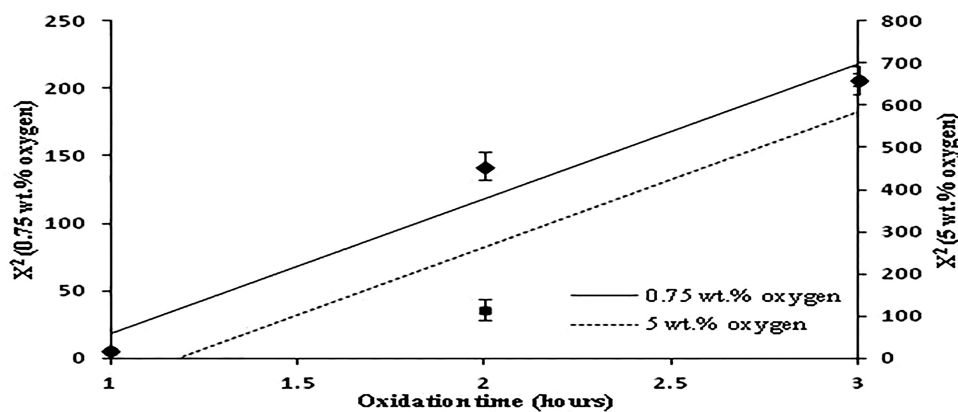


Table 2. The oxide layer thickness, average oxide granule sizes and underwater oil contact angle on C84400 copper alloy samples oxidized in different N₂-O₂ gas mixtures.

N ₂ -O ₂ gas mixture	Oxidation time (t in hours)	Average surface roughness (R _a in μm)	Oxide layer thickness (λ in μm)	Underwater oil contact angle (θ _o)
Polished	0	0.1	-	54° ± 2°
N ₂ -0.75 wt.% O ₂	1	1.13	2.52 ± 0.90	113° ± 9°
	2	1.88	11.94 ± 3.23	119° ± 4°
	3	2.15	14.37 ± 2.07	118° ± 3°
N ₂ -5 wt.% O ₂	1	0.96	4.38 ± 1.63	116° ± 4°
	2	1.11	10.72 ± 5.03	135° ± 3°
	3	2.08	25.69 ± 9.14	154° ± 1°

In the parabolic equation, X , K_p and t are the oxide layer thickness, the oxidation rate constant and the oxidation time, respectively. The resulting oxidation kinetic plots for the growth of the oxide layers are shown in Figure 6.

Figure 6. Plot of the square of the oxide layer thickness against oxidation time.



The rate constant from the curves, $3.0 \times 10^{-4} \mu\text{m}^2 \text{s}^{-1}$ and $8.0 \times 10^{-4} \mu\text{m}^2 \text{s}^{-1}$, were calculated for the samples oxidized in the N_2 0.75 wt.% O_2 and N_2 5 wt.% O_2 gas mixtures, respectively, through the slopes of the plots. This confirms that by increasing the weight percentage of oxygen in the N_2 - O_2 gas mixture, the rate of the oxidation process, through the growth of the oxide layer, increased remarkably.

The thermal oxidation and the growth of the CuO, ZnO and PbO granules sufficiently modified the surface morphology and increased the average surface roughness of the surface. The values of the average surface roughness, R_a , of these thermally oxidized samples were comparable irrespective of the N_2 - O_2 gas mixture used in the experiments, as stated in Table 2. The maximum R_a values of 2.10 μm and 2.08 μm were obtained after 3 h of the thermal oxidation in the N_2 -0.75 wt.% O_2 and N_2 -5 wt.% O_2 oxidizing gas mixtures, respectively. This increase in the values of the average surface roughness and the resulting rough surfaces of the samples are due to the irregular packing, as well as the morphologies of the various oxides that have been formed during the thermal oxidation.

3.4. Underwater Oil Contact Angle Behavior

The polished surface of the C84400 was oleophilic, with an oil contact angle of $54^\circ \pm 2^\circ$. However, after the thermal oxidation process in the N_2 - O_2 gas mixtures, the surfaces became oleophobic, with the underwater oil contact angles showing superoleophobicity with an increase in the thickness of the oxide layers. The contact angle of the oil (θ_o) increased and peaked at $154^\circ \pm 1^\circ$ after 3 h of thermal oxidation in the N_2 5 wt. % O_2 gas mixture.

The roughness of the thermally oxidized surfaces, as well as the surface tension at the oil-oxide interface causes the oleophobicity of the oil contact angles on the samples when placed under water. The oxide layers act as low energy surfaces under water, due to surface tension. The average roughness values, R_a , of the surfaces were comparable irrespective of the N_2 - O_2 gas mixture used. Therefore, the increase in the underwater oil contact angles is dependent on other factors beyond the surface roughness and surface tension effects.

To this end, the underwater oil contact angles, as well as the resultant underwater superoleophobicity can be explained from two perspectives, namely: the low fractional surface area of surfaces, due to the surface morphology of the oxide granules, as well as the porosity of the thermally grown oxide layer of varying thicknesses. Based on the Cassie-Baxter model [20] as stated in Equation (2), the fractional surface area of the oxide granules (f_{so}) in contact with the oil must be small for the surface to exhibit high oil contact angles and superoleophobicity.

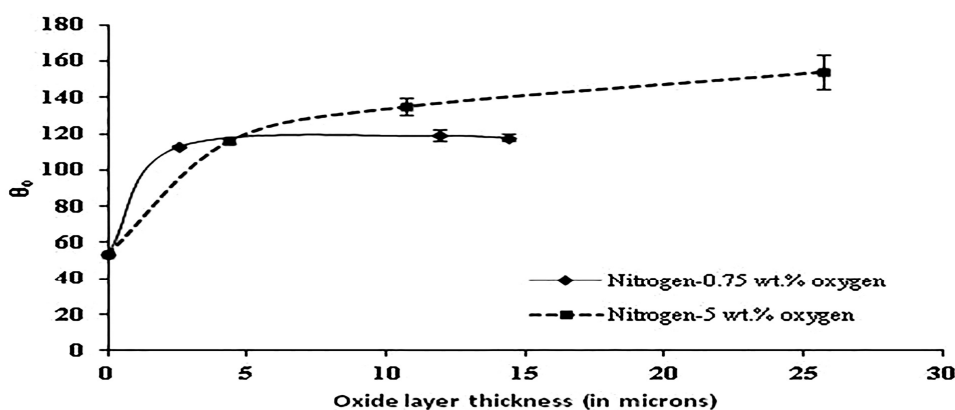
$$\cos \theta_o = f_{so} (\cos \theta + 1) - 1 \quad (2)$$

Using the Cassie-Baxter model, with θ equal to the underwater oil contact angle on the polished C84400 copper alloy surface ($\theta = 54^\circ \pm 2^\circ$) and θ_o equal to the measured underwater oil contact angle values on the thermally oxidized surfaces, the fractional surface areas of the oxide granules were calculated. The calculated values of f_{so} were within the range of 0.32–0.39 and 0.06–0.35 for the C84400 copper alloy samples oxidized in the N_2 -0.75 wt.% O_2 and N_2 -5 wt.% O_2 gas mixtures, respectively, as stated in Table 1. The nano-sized oxides generated hierarchical surface layers, as can be seen in the SEM images, due to their irregular parking and size differences. The small granules of CuO, PbO and ZnO provided a very small surface area for wetting by the oil.

Beyond the small fractional surface area of the oxide granules, the porosity of the oxide layers aided in the increment of the underwater oil contact angles into the superoleophobic region. As stated earlier, there is a pronounced distribution of pores in the samples that were oxidized in the N₂-5 wt.% O₂ gas mixture, as shown by the SEM images in Figure 2e–f. The distribution of the pores was insignificant in the samples that were thermally oxidized in the N₂-0.75 wt.% O₂ gas mixture, due to the morphology of the oxides and the thinness of the oxide layers.

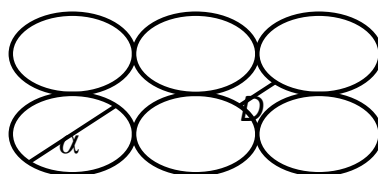
As the thickness of the oxidized surface layer increased to 25.69 ± 9.14 μm, the underwater oil contact angles on the surfaces shifted from oleophobicity to superoleophobicity. This dependence of the underwater oil contact angles with the oxide layer thickness is shown in Figure 7.

Figure 7. Plot of the underwater oil contact angle as a function of the oxide layer thickness.



As can be noted in the plot, the samples oxidized in the N₂-5 wt.% O₂ gas mixture showed underwater superoleophobicity on the thicker oxide scales formed after the 3 h of thermal oxidation. To effectively explain this trend, the porosities of the oxide layers are estimated based on the effective sizes of the pores, *D*, and the average sizes of the oxide granule, *α*. In this case, the porosity of the oxide layers formed after the thermal oxidation of the samples is the ratio of the pore size (*D*) to the sum of the pore size and the sizes of the adjoining oxide granules that creates the pore, as represented below in Figure 8. The oxide granules are assumed to be spherical in shape.

Figure 8. A simple 2D model of the spherical oxide granules of size *α* and pore sizes, *D*.



Based on the above model, the porosity of the oxide layers, ϕ , is given as:

$$\phi = \frac{D}{D + k\alpha} \tag{3}$$

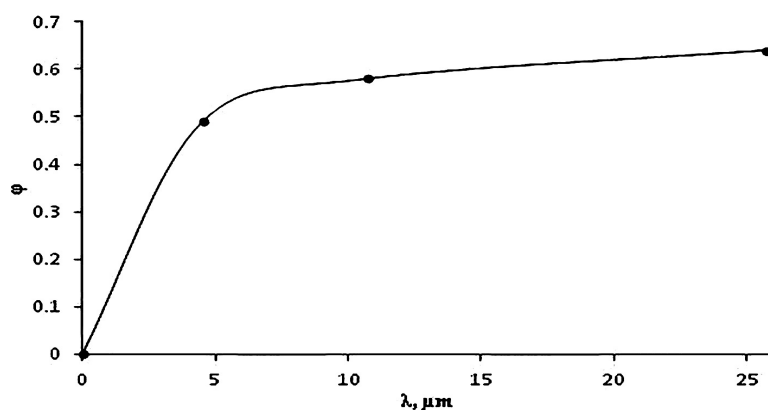
k is the statistical average of the number of oxide granules adjoining a pore. Thus, ϕ is given by Equation (4), with *k* equal to four.

$$\varphi = \frac{D}{D + 4\alpha} \quad (4)$$

The values of experimentally determined D and α , as well as the calculated porosities, φ , are stated in Table 1.

The calculated oxide layer porosities increased with the thickness of the oxide layers. This variation of the porosity, φ , with the oxide layer thickness of the C84400 copper alloy samples that were oxidized in the N₂-5 wt.% O₂ gas mixture is shown in Figure 9.

Figure 9. The plot of the variation of the calculated porosity, φ , against the average oxide layer thickness, λ , for samples thermally oxidized in the N₂-5 wt.% O₂ gas mixture.



The generally well-defined, small oxide granules formed in the N₂-5 wt.% O₂ gas mixture contribute significantly to the porosity, which is stabilized at higher oxide thicknesses. This is not the case with the oxide layer formed during the thermal oxidation in the N₂-0.75 wt.% O₂ gas mixture, where the estimated porosities were very low. This increase in porosity causes more infiltration and trapping of water in the thicker oxide layers, which is necessary to sustain a stable Cassie-Baxter state, needed for underwater superoleophobicity. The spontaneous invasion of these pores takes place through the capillary phenomenon, and the thicker oxide layers, therefore, show underwater superoleophobicity.

4. Conclusions

The thermal oxidation of the C84400 copper alloy followed the parabolic law and was diffusion driven. The X-ray diffraction analyses confirmed that the oxide layers were composed of lead (II) oxide, copper (II) oxide and zinc (II) oxide. The surfaces after the thermal oxidation process had different morphologies, which reduced the fractional surface area, f_{so} , of the oxide grains that is wetted by the oil. The irregular packing of the oxide grains caused the generation of pore spaces on the oxide surface layers of the samples. The porosities of the oxide layers increased with the oxide layer thickness. The underwater oil contact angles increased as the thickness of the porous oxide layers increased for the samples thermally oxidized in the N₂-5 wt.% O₂ gas mixture. At an oxide layer thickness above 25 microns, the measured contact angle exceeded 150°, implying that a stable Cassie-Baxter wetting state was sustained on thicker porous oxide layers.

Acknowledgments

This work was partially supported by the National Science Foundation Industry/University Cooperative Research Center on Water Equipment and Policy located at the University of Wisconsin-Milwaukee and Marquette University (IIP-0968887 and IIP-0968844). The authors also thank Steven Hardcastle of the University of Wisconsin-Milwaukee (UWM) Advanced Analysis Facility for his assistance in the characterization of the samples and Benjamin Schultz for his assistance in sample preparation.

Conflicts of Interest

The authors declare no conflict of interest.

References

1. Kota, A.K.; Tuteja, A. *Advances in Fluorine-Containing Polymers*; Smith, D.W., Ed.; American Chemical Society: Washington, DC, USA, 2012; Volume 1106, Chapter 11, p. 171.
2. Sheparovych, R.; Motornov, M.; Minko, S. Low adhesive surfaces that adapt to changing environments. *Adv. Mater.* **2009**, *21*, 1840–1844.
3. Zhang, L.; Zhang, Z.; Wang, P. Smart surfaces with switchable superoleophilicity and superoleophobicity in aqueous media: Toward controllable oil/water separation. *NPG Asia Mater.* **2012**, *4*, e8.
4. Yao, X.; Gao, J.; Song, Y.; Jiang, L. Superoleophobic surfaces with controllable oil adhesion and their application in oil transportation. *Adv. Funct. Mater.* **2011**, *21*, 4270–4276.
5. Tuteja, A.; Choi, W.; McKinley, G.H.; Cohen, R.E.; Rubner, M.F. Design parameters for superhydrophobicity and superoleophobicity. *MRS Bull.* **2008**, *33*, 752–758.
6. Wu, W.; Wang, X.; Wang, D.; Chen, M.; Zhou, F.; Liu, W.; Xue, Q. Alumina nanowire forest via unconditional anodization and super-repellency plus low adhesion to diverse liquids. *Chem. Commun.* **2009**, *9*, 1043–1045.
7. Tian, D.; Zhang, X.; Tian, Y.; Wu, Y.; Wang, X.; Zhai, J.; Jiang, L. Photo-induced water–oil separation based on switchable superhydrophobicity–superhydrophilicity and underwater superoleophobicity of the aligned ZnO nanorod array-coated mesh films. *J. Mater. Chem.* **2012**, *22*, 19652–19657.
8. Liu, X.; Gao, J.; Xue, Z.; Chen, L.; Lin, L.; Jiang, L.; Wang, S. Bioinspired oil strider floating at the oil/water interface supported by huge superoleophobic force. *ACS Nano* **2012**, *6*, 5614–5620.
9. Liu, X.; Zhou, J.; Xue, Z.; Gao, J.; Meng, J.; Wang, S.; Wang, S.; Jiang, L. Clam’s shell inspired high-energy inorganic coatings with underwater low adhesive superoleophobicity. *Adv. Mater.* **2012**, *24*, 3401–3405.
10. Lin, L.; Liu, M.; Chen, L.; Chen, P.; Ma, J.; Han, D.; Jiang, L. Bio-inspired hierarchical macromolecule–nanoclay hydrogels for robust underwater superoleophobicity. *Adv. Mater.* **2010**, *22*, 4826–4830.
11. Anzel, I. High temperature oxidation of metals and alloys. *Metal. J. Metall.* **2011**, *13*, 325–336.

12. *ASM Specialty Handbook: Copper and Copper Alloys*; Davis, J.R., Ed.; ASM International: Russell, OH, USA, 2001.
13. Kirschner, C.M.; Brennan, A.B. Bio-Inspired antifouling strategies. *Annu. Rev. Mater. Res.* **2012**, *42*, 211–229.
14. Wagner, C. Theoretical analysis of the diffusion processes determining the oxidation rate of alloys. *J. Electrochem. Soc.* **1952**, *99*, 369–380.
15. Shackelford, J.M.; Alexander, W. *CRC Materials Science and Engineering Handbook*; CRC Press: New York, NY, USA, 2010; pp. 220–221.
16. Carter, C.B.; Norton, M.G. *Ceramic Materials: Science and Engineering*; Springer: New York, NY, USA, 2013; pp. 628–629.
17. Dzhaforov, T.D.; Altunbas, M.; Gorur, O. The high-temperature thermal expansion of BiPbSrCaCuO superconductor and the oxide components (Bi₂O₃, PbO, CaO, CuO). *J. Mater. Sci.* **1996**, *31*, 2207–2212.
18. Walsh, R. *Electromechanical Design Handbook*; McGraw-Hill: New York City, NY, USA, 2000; Chapter 4, pp. 19–20.
19. Xu, C.H.; Zhu, Z.B.; Lui, H.F.; Lui, C.; Surya, S.Q. The effect of oxygen partial pressure on the growth of ZnO nanostructure on Cu_{0.62}Zn_{0.38} brass during thermal oxidation. *Superlattices Microstruct.* **2011**, *49*, 408–415.
20. Cassie, A.B.D.; Baxter, S. Wettability of porous surfaces. *Trans. Faraday Soc.* **1944**, *40*, 546–551.

© 2014 by the authors; licensee MDPI, Basel, Switzerland. This article is an open access article distributed under the terms and conditions of the Creative Commons Attribution license (<http://creativecommons.org/licenses/by/3.0/>).